Electrochimica Acta 398 (2021) 139205

Contents lists available at ScienceDirect

Electrochimica Acta

journal homepage: www.elsevier.com/locate/electacta

Isolation of competing morphological patterns during microfluidic electrodeposition: Experimental confirmation of theory

Sarathy K. Gopalakrishnan[a,b], Akash Ganesh[a], Chun-Chieh Wang[a], Matthew Mango[a], Kirk J. Ziegler[a,1,*], Ranga Narayanan[a,1,*]

[a] Department of Chemical Engineering, University of Florida, Gainesville, Florida 32611, USA
[b] Department of Materials Science and Engineering, University of Florida, Gainesville, Florida 32611, USA

ARTICLE INFO

Article history:
Received 4 June 2021
Revised 16 August 2021
Accepted 28 August 2021
Available online 6 September 2021

Keywords:
Instability
Perturbation
Image Processing
Pattern recognition
Fast Fourier Transform

ABSTRACT

Small disturbances at an interface can lead to well-defined patterns in many systems. However, nonlinear interactions obscure the dominant wavelength in the instability pattern of diffusion-limited systems, which has limited the study of these systems. The design of a microfluidic cell that mitigates nonlinear effects is presented, enabling enhanced diffusional effects and quasi-1D electrodeposition of patterns on the cathode. These microfluidic cells, operating at small overpotentials, were able to isolate morphological patterns during electrodeposition. An automated image analysis routine is developed to convert the instability pattern into a height profile and objectively extract the wavelengths composing the pattern. Although multiple wavelengths, including harmonics, were observed in the pattern, a custom, directed filter was applied across the spectrum to identify noise and select the dominant wavelength from the pattern. The dominant wavelength of nearly all experiments were within 5% of the theoretical wavelength and two-thirds were within 1%.

1. Introduction

Interfacial instability occurs in many processes as a result of disturbances growing at an interface [1–14]. These instabilities are typically characterized by the formation of a well-defined pattern that forms due to the presence of potential gradients from an applied difference in temperature, concentration, pressure, or electrochemical potential [5,8,15–17]. Phase-change processes are diffusion-limited and often lead to potential gradients and instabilities. However, it has been more difficult to characterize and attain the dominant wavelength of these instabilities due to the broad growth curves associated with these systems. The lack of a well-defined dominant wavelength leads to nonlinear interactions that manifest as dendrites commencing from structural inhomogeneity in the solid or fluctuations in the concentration or temperature field in the fluid [8,18–20].

In electrochemical systems, periodic instability patterns have been observed at the electrode during electrodeposition [19,21–26] but determination of the dominant wavelength has been obscured by the rapid formation of dendrites and the 2D nature of the electrode. The random disturbances associated with an instability are driven by the potential gradients while the wavelengths of the ensuing interfacial cellular patterns are regulated by diffusional gradients transverse to the growth direction and by surface energy between the solid and fluid [27,28]. Although other works have observed morphological patterns during electrodeposition [21,23,26,29], these studies focused on overall growth rate rather than isolating the wavelength of the instability.

Developing the experimental protocols necessary to isolate morphological patterns in diffusion-limited systems was difficult and only realized once we developed the quasi-1D electrodes with narrow spacings described in this manuscript. The electrochemical cell designed to study these systems enhances the competition between the forces at the surface and enables the formation of the dominant wavelength in a shorter experimental time frame, i.e., delays the onset of dendrite formation. In addition, the quasi-1D nature of the microfluidic cell eases determination of the patterns formed by restricting growth to one focal plane. A custom noise filter is required to analyze the observed wavelengths from the Fast Fourier Transform (FFT) spectrum and select the dominant wavelength from the experiment. These experimental protocols isolated a relatively narrow range of wavelengths associated with the instability. To our knowledge, this work is the first to experimentally quantify wavelengths due to a diffusion-limited instability. The ability to attain defined patterns close to the dominant

* Corresponding authors.
E-mail addresses: kziegler@che.ufl.edu (K.J. Ziegler), ranga@ufl.edu (R. Narayanan).
[1] Postal address: 1006 Center Drive, Office: CHE 404, Gainesville, FL 32611, USA

https://doi.org/10.1016/j.electacta.2021.139205
0013-4686/

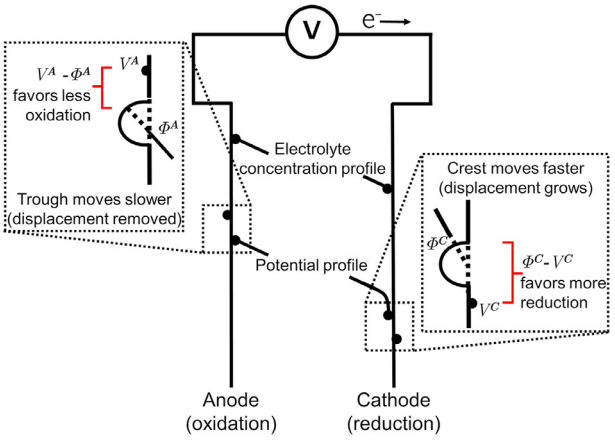

Fig. 1. Schematic of the potential and electrolyte concentration in an electrodeposition system. The zoom boxes illustrate the scenario when a disturbance is added to the electrode surface. Here V and ϕ denote the electrical and solution potential, respectively, while the superscripts A and C represent the anode and cathode, respectively.

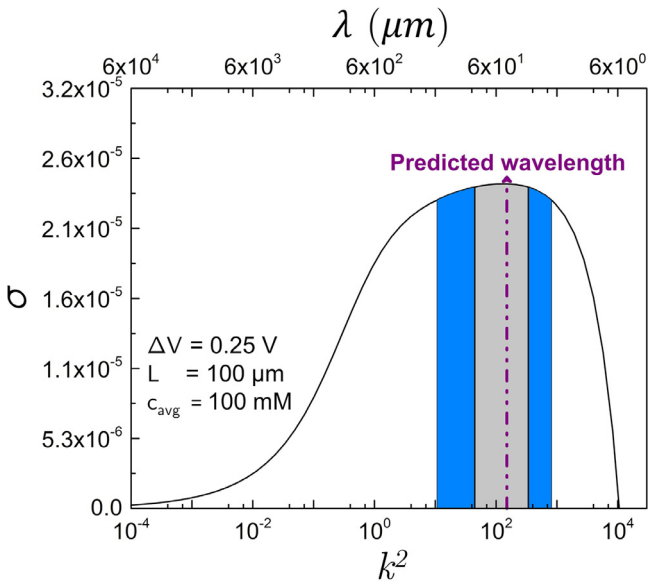

Fig. 2. Dimensionless growth rate (σ) vs. wavenumber squared (k^2) plot. The dimensionless constants are $\mathcal{A} = 4.03 \times 10^{-5}$, $\mathcal{B} = 27.02$, $\mathcal{C} = -882.353$, and the growth speed is $U = 0.099$, as discussed further in the SI Appendix. The wavelength corresponding to the maximum growth rate predicted by the model is shown as well as the wavelength range within 1% (gray region) and 5% (blue region) of the maximum growth rate. (For interpretation of the references to color in this figure legend, the reader is referred to the web version of this article.)

wavelength enables comparison to theoretical models describing the onset of the instability [27]. Understanding and manipulating the patterns formed during electrodeposition enables the tuning of structures for MEMS (micro-electromechanical systems) fabrication and may also be extended to measure the interfacial energy between solids and liquids [30–33].

Metal deposition on an electrode occurs when an electrical potential is imposed across two metal surfaces that are separated by an ionic solution. A typical electrodeposition system is composed of a flat anode, a flat cathode, and an ionic electrolyte solution between the two, as depicted in Fig. 1. When a voltage drop is imposed across the two metal electrodes, chemical reactions commence at the surface (see Fig. 1). At the anode, the metal is oxidized to metal ions and electrons. These electrons are then conducted through a wire that connects the electrodes, while the charge is carried by the ions that migrate and diffuse through the electrolyte toward the cathode. At the cathode, the ions are reduced by the electrons to elemental metal. In other words, the anode dissolves and the cathode grows in an electrodeposition process. The reactions establish an electrochemical potential gradient in the solution as well as a concentration gradient.

When the potential difference exceeds a critical value, the planar electrode surfaces will become wavy due to an interfacial instability [15,34–37]. To understand why this occurs, consider the local surface morphology at the electrode depicted in the schematic of Fig. 1. Any disturbance on either the anode or cathode alters the potential profile locally. These changes to the profile can either enhance or hinder reactions at the surface. A perturbation at the anode causes the difference in potential between the solution and electrode to decrease, which reduces oxidation of the metal and the ultimate elimination of any disturbance. The opposite occurs at the cathode where the altered potential profile results in a larger driving force for reduction and deposition. This increased reduction in potential leads to enhanced growth of the perturbation on the cathode. Therefore, any perturbation at the cathode will be self-reinforcing and will grow while the corresponding perturbation at the anode will decrease. This process results in a positive feedback between random disturbances at the electrode and the ion concentration as well as electrochemical potential gradients at the electrode surface.

The perturbations at the surface may be associated with physical differences, such as surface roughness or crystallographic orientations, and localized effects, such as alterations in surface states or transport at the surface. These perturbations occur randomly across the electrode. However, the feedback mechanism encourages prominent patterns at the cathode-electrolyte interface while the anode surface is almost unaffected by comparison. The pattern at the cathode is selected by the competition between stabilizing and destabilizing effects that accentuate the growth of an instability at a dominant wavelength or range of wavelengths.

While the destabilizing effects are due to diffusional gradients, they are countered by the stabilizing effect offered by the curvature of the surface. These stabilizing effects change the energy of activation for the electrochemical reaction, weakening the rate of metal deposition at a crest at the cathode and enhancing it at a trough at the anode (see Fig. 1). The destabilizing effects are independent of the disturbance wavenumber, k, which, in turn is inversely proportional to the disturbance wavelength. The stabilizing effect of curvature, however, is k-dependent [27]. Thus, the wavelength selection in electrodeposition owes its origins to the surface energy of the metal in the presence of the electrolytic solution. Denoting the linear growth rate of a disturbance by σ, several theories have been developed for σ vs. k^2 curves [21–23,26–28,38,39], such as that shown in Fig. 2. A typical σ vs. k^2 curve in electrodeposition initially increases, reaches a maximum, and then decreases, crossing zero at a critical value of k^2 called the neutral point. Beyond the neutral point, disturbances of all wavenumbers are stable with their corresponding growth rates, σ, being negative.

Past workers [27,28] have developed a two–electrode model for obtaining the σ vs. k^2 curves by noting that there are three input variables, *viz*., the average metal ion concentration, the spacing between the electrodes, and the input voltage difference applied across the electrodes. A heuristic model [27] that assumes fast interfacial dynamics relative to domain inertia yields a surprisingly simple formula with high accuracy for the growth rate as a function of wavenumber. This model, discussed in the context of the current work in sufficient detail in the SI Appendix, is typically applicable to electrodeposition cells with electrolyte depths that are small enough to make the diffusional rates large

compared to kinetic rates of ionic transport. Three key dimensionless groups evolve from this model, termed $\mathcal{A}$, $\mathcal{B}$, and $\mathcal{C}$. They represent the scaled interfacial energy, scaled ratio of diffusive to kinetic timescale, and scaled ratio of diffusive to limiting electrode speed. Fig. 2 depicts the dimensionless growth rate (σ) vs. wavelength (or σ vs. k^2) curve obtained from the model for one specific condition, *viz*., 0.25 V applied voltage, 100 μm electrode spacing, and 100 mM ion concentration in a copper–copper sulfate system. The curve shows that every wavelength has a corresponding growth rate, but the expected wavelength observed in experiments would be predicted by the maximum growth rate. Unfortunately, the σ vs. k^2 curve is broad (even in log-scale) near the growth rate maximum. Therefore, long timescales would be required to observe the predicted wavelength, increasing the likelihood of nonlinear interactions that lead to dendrite formation. To avoid these nonlinear interactions, shorter timescales are preferred but several wavelengths with comparable growth rates will still be observed. These short timescale experiments result in electrodeposition patterns having a composition of wavelengths that grow simultaneously. The predicted wavelength with the maximum growth rate, thus, may not be observed in the deposited pattern of an experiment. Based on this conclusion, a pattern composed of just one dominant wavelength, as found in other instability problems, is not likely to be observed [1,2,15,40]. Instead, it is more reasonable to expect that the pattern is composed of a range of wavelengths closer to the predicted wavelength. The goal of the current work is to experimentally validate this theory. To this end, we describe the validating experiments in detail with an interpretation of the observations. To provide meaningful comparison to theory, the wavelength composition obtained from the experiment will be compared with the wavelength range derived from the model within 1 to 5% of the maximum growth rate, as depicted by the shaded areas of Fig. 2.

2. Experiments and methods

2.1. Materials

Borosilicate glass substrates for electrochemical cell fabrication were purchased from Fisher Scientific.® All the chemicals involved in the electrode cell fabrication were purchased from MicroChemicals®, and the fabrication was performed in a Class 100 cleanroom at the Nanoscale Research Facility of the University of Florida. Copper sulfate stock solution was prepared using copper sulfate pentahydrate crystals purchased from Sigma Aldrich.® For electrodeposition experiments, concentrations of 25, 50, and 100 mM were prepared by diluting the 1 M stock solution.

2.2. Fabrication of microfluidic electrochemical cells

The electrodeposition experiments were conducted in a miniaturized electrochemical cell consisting of two copper electrodes with a precise spacing. Photolithography techniques were used to fabricate high precision cells with narrow electrode spacings. Before fabrication, the glass substrates were cleaned in a warm NMP (N-Methyl-2-pyrrolidone) solution held at 70 °C for 5 min to remove any grease/dirt, followed by plasma ashing to remove any residue. The clean glass was then spin-coated (Suss Microtec Delta 80RC) with 2 μm thick AZ1512, a positive photoresist layer, and soft baked for 30 min at 105 °C in an oven to evaporate the solvent. With the desired pattern mask, the photoresist layer was exposed to UV light (365 nm wavelength) for 30 s using a Karl Suss MA-6 contact aligner. Once exposed to UV light, the photoresist coated glass slides were developed in AZ 300MIF solution for 75 s, cleaned with DI water, and dried with nitrogen gas to attain the patterned photoresist layer. The developed photoresist was then plasma ashed once again for 60 s to remove any polymer residue on the photoresist sidewalls. Metal layers were deposited on the patterned photoresist using a Kurt J. Lesker Multi-Source RF and DC Sputter System at the rate of 4 to 5 $Å s^{-1}$. A 100 nm thick adhesion layer of chromium was deposited on the glass and subsequently followed by deposition of a 1 μm layer of copper. After sputter deposition, lift-off was completed in acetone solution for 20 min to get the final electrode design. Several electrochemical cells were fabricated simultaneously on a glass substrate during the fabrication process. A glass cutter was used to separate individual cells from the substrate. The photolithography approach leads to a precise spacing between the two copper electrodes, where one electrode serves as a cathode and the other as an anode. Top-down SEM images of the electrodes demonstrate a precise spacing of 100 μm between them at a precision of ±0.3 μm.

2.3. Electrodeposition of copper

Electrodeposition was carried out by placing the electrochemical cell on a polycarbonate holder with copper tape attached along the electrodes to allow connections to an external circuit. The copper tapes were covered with polyimide tape to avoid any contact with the electrolyte solution. A cover glass was clipped over the electrochemical cell and the copper sulfate electrolyte solution was injected in the gap between the electrodes and cover glass while the cell ends were sealed with epoxy. To minimize convection due to gravity, the setup was kept horizontal using a bubble leveler.

The electrodes were connected to a potentiostat (AUTOLAB PGSTAT30) configured for a two-electrode cell setup to control the input applied voltage between 0.2 and 0.3 V (accuracy: ±0.2% of maximum potential range) and to record the output performance. A conducting wire was used to connect the potentiostat to the electrodes at multiple points to maintain equipotential throughout the deposition. A constant applied voltage was maintained across the electrodes to drive the electrodeposition. The electrochemical setup was located under a microscope with a camera to observe and capture images of the growth patterns during deposition. An objective lens with a magnification of 20× was used for imaging, yielding a pixel resolution of 0.52 μm/pixel. A series of images was taken at constant intervals throughout the experiment for analysis using a programmed image analysis routine.

2.4. Image analysis

Image noise is an aspect of electronic noise that exists in the final images. In the image analysis routine, the image noise is transformed from the original image to the height profile obtained by integrating the binarized image. When FFT is performed on the height profile, frequencies are distributed over the entire FFT spectrum. In many of the images of this study, the initial FFT identified around two thousand frequencies across the entire spectrum of the FFT with magnitudes ranging between zero to ten thousand. The images, such as Fig. 7, show that there are clearly periodic structures, indicating that the waves are obscured by noise occurring across the entire spectrum. Standard FFT filters [41] like high, low, and bandpass filters indiscriminately block frequencies below, above, or within a range of cut-off limits and result in loss of information. These types of filters work well when the signal is known to exist within a defined frequency region. Although our model provides a basis for this region, these filters could introduce significant bias into the analysis. To remove the image noise spread randomly across the entire FFT spectrum, a directed filter is needed that scans the full spectrum and carefully analyzes the potential noise at each frequency before eliminating it from further analysis. In this work, we developed a three-step process to remove frequencies across the entire FFT spectrum, consisting of a custom

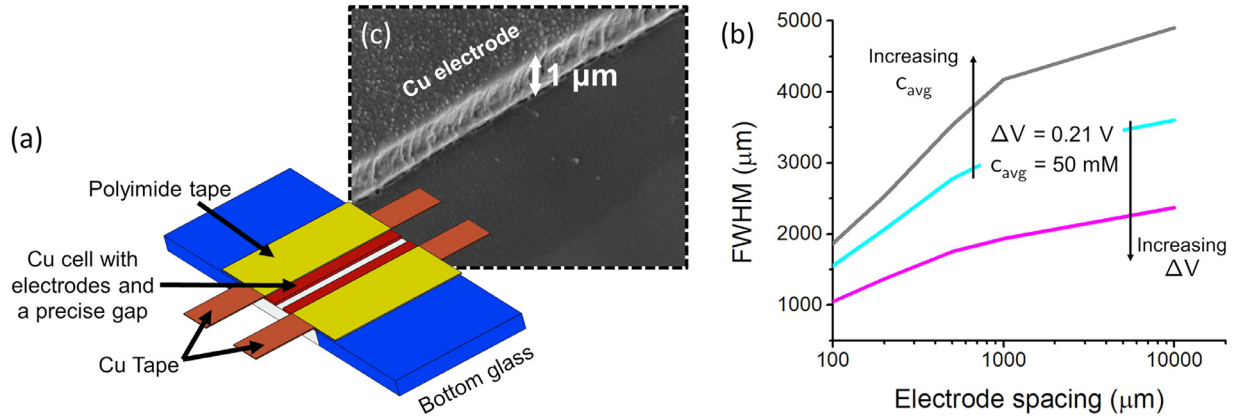

Fig. 3. The microfluidic electrochemical cell consists of copper electrodes connected to copper tape. (a) Polyimide tape sealed the cells with a cover glass (not shown) so that patterns could be observed under a microscope. (b) Model calculations demonstrate the influence of spacing between the metal electrodes, the applied voltage across the electrodes, and the concentration of the electrolyte solution on the FWHM dispersion of the growth rate curve (σ vs. k^2). (c) Lithography enabled precise formation of thin electrodes enabling quasi-1D electrodeposition of copper.

FFT filter, defining the proper noise region for a SNR (signal-to-noise) filter, and identifying the minimum distance separating distinct waves. The first step was based on analyzing each frequency one at a time to determine its relevance in the overall signal. The latter steps are specified by the image resolution. Details on the operations of the filters are given in the SI appendix.

2.4.1. Generation of height profile

The color image in Fig. 4(a) is first converted to a grayscale image, as shown in Fig. 4(b), and the region of interest (cathode with the patterns) is selectively cropped, as shown in Fig. 4(c). Following this step, binarization [42] is performed on the grayscale image to transform the 0–255 spectrum of grayscale to 0–1 binary spectrum, as shown in Fig. 4(d). The binary value of each pixel is determined by the threshold set by an in-built adaptive threshold function [43]. Pixels associated with the copper electrode and instability pattern with grayscale values lower than the threshold were assigned to black (i.e., value of 0) while others were assigned to white (i.e., value of 1). The number of contiguous black pixels in each column of pixels across the image width, *n*, is integrated to generate the height profile from the binarized image.

2.4.2. Development of custom FFT filter

The custom FFT filter iterates through the FFT spectrum and assesses the importance of each frequency in building the height profile. The filter operates by cycling through the FFT spectrum and assigning the magnitude to zero for each frequency one at a time, thus, having some similarities to bootstrapping methods [44]. After zeroing the magnitude of a frequency, the filter performs an inverse transformation on this new FFT spectrum. The mean percentage error is calculated between the new inverse transform and the height profile. If the mean percentage error is more than a threshold limit, which was defined to a value of 0.3%, the filter keeps the original magnitude for that frequency unaltered. If the error introduced by negating the frequency is below the threshold, the frequency is eliminated from the FFT spectrum. The filter performs this analysis on all frequencies and their magnitudes by cycling through the entire FFT spectrum. After the custom filter was used, the modified and the original height profile were compared to ensure the variation was acceptable (see Fig. 4(f)).

2.4.3. Definition of the noise region for SNR filter

Many filters are based on whether the signal is significantly greater than the noise. These SNR (signal-to-noise ratio) filters calculate the SNR of a peak by dividing the signal magnitude by the noise amplitude. A common threshold of a SNR filter is a ratio of 3 [45–48]. Therefore, all peaks with a SNR of more than 3 are identified as significant signals and used in the subsequent analysis. In order to properly apply a SNR filter, one must have an understanding of the region of the FFT associated with noise or have signals that are substantially above the threshold. In this study, images need to be captured at the early stages of growth to adequately capture the forces responsible for the instability. However, the true signals within the FFT are not easily distinguished from the noise region at these early stages.

In order to determine the region of the FFT spectrum associated with noise for our electrodeposition studies, we must first define what constitutes the smallest observable wavelength (signal). These smallest wavelengths (highest frequencies) are defined by the pixel resolution. As shown in Fig. S2(a), at least 4 pixels in width are required to form a distinct half-wave from an image. Any wave shorter than 4 pixels in width would have adjacent pixels with grayscale values that would be indistinguishable. Since the pixel resolution of all images used in this study is 0.52 µm/pixel, the smallest measurable wavelength in this study is 4.16 µm. Therefore, a well-defined noise region exists at the tail of the FFT spectrum. We chose the noise region cutoff to be 2× the smallest measurable wavelength. This region corresponds to a maximum wavelength of 8.32 µm or 0.5% of the largest wavelength attainable by our images. In the frequency domain, the background noise region corresponds to all frequencies beyond 0.0625, which is the region where the FFT magnitude vs. frequency trend is flat, as shown in Fig. S2(b). The noise amplitude of the SNR has a value corresponding to the highest peak of the FFT spectrum within this region.

2.4.4. Identification of the minimum observable distance between waves

Following the custom FFT and SNR filtering steps, the FFT spectrum still contains many wavelengths/frequencies that could describe the instability pattern. Although a composition of wavelengths would be expected due to the flat growth curve and early timescales applied for analysis, many of the peaks have wavelengths that differ by only a few microns. Image artifacts associated with the pixel resolution can yield peaks with similar wavelengths, which are likely different representations of the same wave. Similar to how the pixel resolution limits the smallest quantifiable wave, pixel resolution also determines the smallest measurable distance between two waves.

As shown in Fig. S2(c), two waves can be identified as unique waves only if their peaks are separated by a distance equivalent to at least 3 pixels in width. This represents the smallest $\Delta\lambda$ that

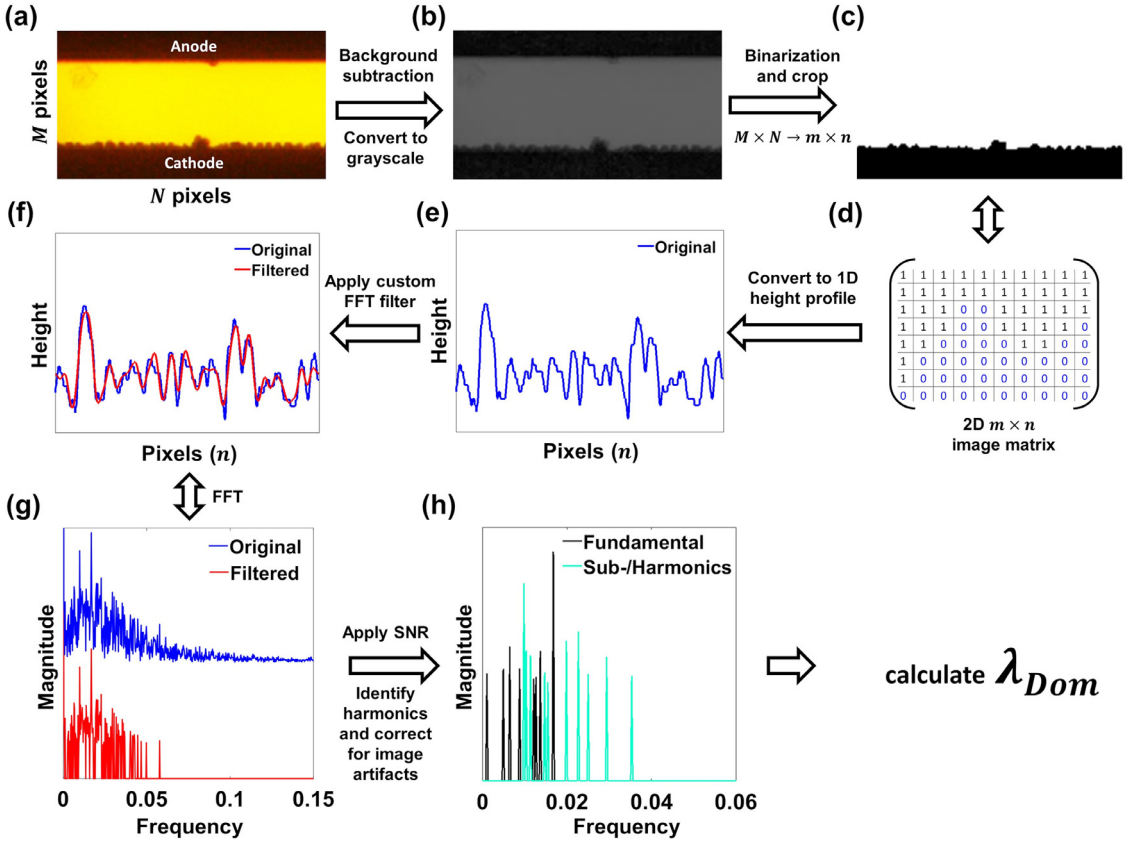

Fig. 4. Schematic of the image analysis routine used for determining the wavelength composition of the electrodeposition pattern. (a) Original image of the electrodeposition pattern captured before the onset of non-linear dendritic growth. (b) The background is subtracted and the image is converted to grayscale. (c) The grayscale image is then cropped from a size of $M \times N$ to $m \times n$ to only show the cathode portion with the instability pattern (where M and N, and m and n are the height and width of the image before and after cropping, respectively). (d) The cropped image is binarized using an adaptive threshold function and converted to a 2D image matrix. (e) The contiguous black pixels in each column of pixels across the image width (n) are integrated to generate the height profile. (f) The original height profile (blue) is compared to the new height profile (red) after applying the custom filter. (g) The new height profile is converted to frequencies using FFT. The spectrum of the new height profile (red) is compared with the spectrum of the original height profile (blue) with noise. (h) The number of frequencies are reduced by comparing each to the SNR and eliminating frequencies associated with image artifacts. Only peaks with an SNR greater than 3 are shown for the fundamental (black) and sub-/harmonic wavelengths (green). The dominant wavelength is calculated by taking an average of all the remaining wavelengths weighted with their respective magnitudes. (For interpretation of the references to color in this figure legend, the reader is referred to the web version of this article.)

can be accurately measured by the FFT analysis. For the images of this study, $\Delta\lambda$ corresponds to a wavelength of 1.56 μm. Therefore, peaks with similar wavelengths separated by a distance less than 1.56 μm were considered one peak and combined into one wavelength/frequency with a magnitude equivalent to the peak with the highest magnitude in that set. For example, five peaks may be observed with wavelengths of 44, 44.5, 45, 46.9, and 50 μm corresponding to magnitudes of 100, 200, 400, 650, and 500, respectively. The first four waves are indistinguishable from one another since the separation distance between the consecutive peaks is less than 1.56 μm. Therefore, the first four peaks are considered as the same wave with one unique wavelength. Among the four, the 46.9 μm peak has the highest magnitude in the set and will be taken as the unique wavelength of the peak.

2.5. Selection of dominant wavelength

Application of the three filters described above significantly narrows the number of frequencies attained from the FFT analysis. The remaining waves cover a broad range of wavelengths/frequencies with different magnitudes. Due to this broad range, the composition of wavelengths can include sub-/harmonics that complicate the analysis of the predicted wavelength representing the wave with the maximum growth rate (see Fig. 2). In addition, the short timescales of the experiments suggests that many fundamental wavelengths near the predicted wavelength may still exist. Fig. S1 compares the full composition of wavelengths (fundamental wavelengths and their sub-/harmonics) obtained for each experimental condition to its theoretical wavelength predicted by the model. The size of each data point corresponds to their respective FFT magnitude. The identity line marks the predicted wavelength with maximum growth rate derived from the model for different experimental conditions. Although the model results could be used again to exclude specific wavelengths/frequencies from further analysis, it would bias the results to the anticipated wavelength. For this reason, all of the wavelengths were included in determining a dominant wavelength (λ_{Dom}), which was calculated for each experimental condition by performing a weighted average of the full composition of the wavelengths in Fig. S1 (including sub-harmonics and harmonics) by their respective magnitudes. For easier comparison between two data sets, Fig. 8 of the manuscript is plotted with only the dominant wavelength and confidence intervals.

3. Results and discussion

The electrodeposition experiments in this study were conducted in a microfluidic electrochemical cell consisting of two copper electrodes with a precise spacing determined by lithography. Fig. 3(a)

shows the basic construction of the electrochemical cells. Fig. 3(b) presents the calculated dispersion in the growth rate curve (e.g., σ vs. k^2 plot of Fig. 2) for the morphological patterns as a function of the spacing between the metal electrodes (L). At the same potential, the spacing between the electrodes has a dramatic influence on the full width at half maximum (FWHM). A change from 1 cm to 100 μm reduces the FWHM by more than 50%. Lower electrolyte concentration and higher potentials (ΔV) also reduce the FWHM of the growth rate curve. These calculations suggest that low concentrations, large potentials (within the range defined by the physics), and narrow electrode spacings would provide the desired conditions to minimize the number of observed wavelengths. Another key aspect of the electrochemical cells is the quasi-one-dimensional growth enabled by the use of thin electrodes (1 μm thick), as shown in Fig. 3(c).

The control input parameters for the electrodeposition experiments were the applied voltage across the electrodes, the mean concentration of the electrolyte solution (c_{avg}), and the spacing between the metal electrodes. The experimental output variables were the total current and the electrode morphology or pattern. The pattern morphology and its wavelength decomposition is used for comparison to the theory. The activation over-potential of the copper–copper sulfate system was measured to be around 200 mV. The voltage used in the theoretical models, i.e., the Butler-Volmer equation, is the difference between the applied voltage and the measured activation overpotential.

Fig. 4 (a) shows the image of the electrodeposition pattern captured soon after the instability commences and well before the onset of nonlinear interactions that depict dendritic growth. Note that these patterns form at different operating conditions and wavelengths than those observed in hydrodynamic instabilities [49–51]. The instability pattern seen here is a superimposition of multiple wave patterns with unique wavelengths. An image analysis routine was developed using MATLAB® to objectively and reliably extract the wavelength composition from the electrodeposition patterns. In this automated routine, we convert the electrodeposition pattern into a height profile and decompose it using FFT to extract information about the wavelength composition and growth rate.

Fig. 4 (b)–(d) shows the steps involved in the image processing to convert the image to a height profile. The purpose of these image processing steps is to generate a height profile of the electrodeposition patterns by distinguishing the copper portion (cathode and the instability patterns) from the electrode gap. Fig. 4(e) shows the height profile obtained by integrating the binarized image. In the next step shown in Fig. 4(f), the height profile is decomposed using the FFT algorithm [41,52], and the information about the wavelength and growth rate is expressed in terms of magnitude vs. frequency plots, as seen in Fig. 4(g). Here, the frequency is the inverse wavelength (frequency = pixel resolution/wavelength, where pixel resolution is 0.52 μm). The magnitude represents the amplitude of each wave pattern, where waves with the fastest growth rates will have larger amplitudes/magnitudes. Conversely, the original height profile can be retrieved by performing an inverse transform on the FFT data (see Fig. 4(f) to compare the original and modified height profile).

In the raw FFT data, frequencies associated with image noise as well as the desired signals are distributed over the entire FFT spectrum. In the FFT spectrum, the magnitude of the noisy frequencies is nulled using a custom filter developed in this work. Briefly, each frequency is removed to determine its independent effect on the overall reconstructed height profile, enabling removal of many frequencies that do not contribute to the pattern. Fig. 4(g) shows the magnitude vs. frequency plot for the raw FFT and noise-filtered FFT spectrum. In addition to the custom filter, a SNR (signal-to-noise ratio) filter with a value of 3 is applied to identify the peaks

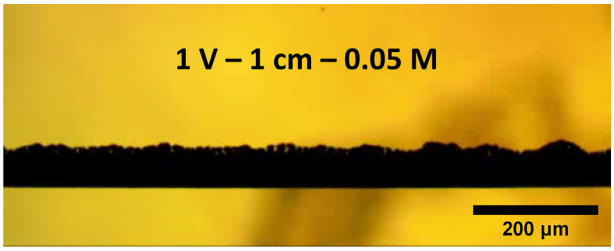

Fig. 5. The evolution of electrodeposition patterns in a 1 cm electrode spacing cell operated at an applied voltage of 1 V and a mean electrolyte concentration of 50 mM. The anode is not in the field of view of the camera. The corresponding video (at 60× speed) is available as supplemental material.

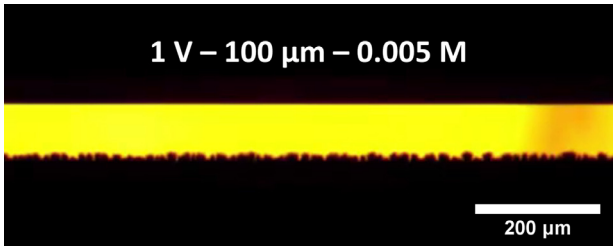

Fig. 6. The evolution of electrodeposition patterns in a 100 μm electrode spacing cell operated at an applied voltage of 1 V and a mean electrolyte concentration of 5 mM. The corresponding video (at 5× speed) is available as supplemental material.

with significant signals [45–48]. The noise amplitude of the SNR has a value corresponding to the highest peak of the FFT spectrum within the background noise region (SI appendix, Fig. S2), which was determined to be above a frequency of 0.0625 in the FFT plot shown in Fig. 4(g).

Once the noise frequencies are filtered and peaks with significant signals are identified, we get a composition of wavelengths that form the instability patterns. However, image artifacts associated with pixel resolution yield some peaks with very similar wavelength. These different wavelengths are likely different representations of the same wavelength. Since the pixel resolution limits the smallest measurable distance between two peaks (SI appendix, Fig. S2), peaks separated by fewer than 3 pixels (equivalent to 1.56 μm) are considered one wavelength and combined into one frequency. In addition to these image artifacts, the scale of the image enables the observation of sub-harmonics and/or harmonics of the fundamental frequency. Therefore, the fundamental wavelength (F) and their respective harmonics are also isolated based on their magnitude. The sub-harmonics have wavelengths that are integer multiples (kF) of the fundamental wavelength while the harmonics have wavelengths that are $1/k^{th}$ of F. After identifying a harmonic family, the peak with the highest magnitude in the group was selected as the fundamental wavelength. Fig. 4(h) shows the final frequencies/wavelengths that compose the pattern observed in the image of Fig. 4(a). The dominant wavelength within this composition of wavelengths is determined by performing a weighted average (including sub-harmonics and/or harmonics) of all wavelengths weighted with their respective magnitudes, $\lambda_{Dom} = \sum M_i^{-1} \cdot \sum M_i \cdot \lambda_i$ where M_i is the magnitude of the peak corresponding to wavelength λ_i. The dominant wavelength obtained from each experiment is then compared to the predicted wavelength with the maximum growth rate derived from the model.

Figs. 5 and 6 depict the evolution of patterns for cells with 1 cm and 100 μm spacing operated under an applied voltage of 1 V and mean electrolyte concentration of 50 mM and 5 mM, respectively. For the larger electrode spacing (Fig. 5), the instability is limited by diffusional transport. Wavelengths that form the patterns compete

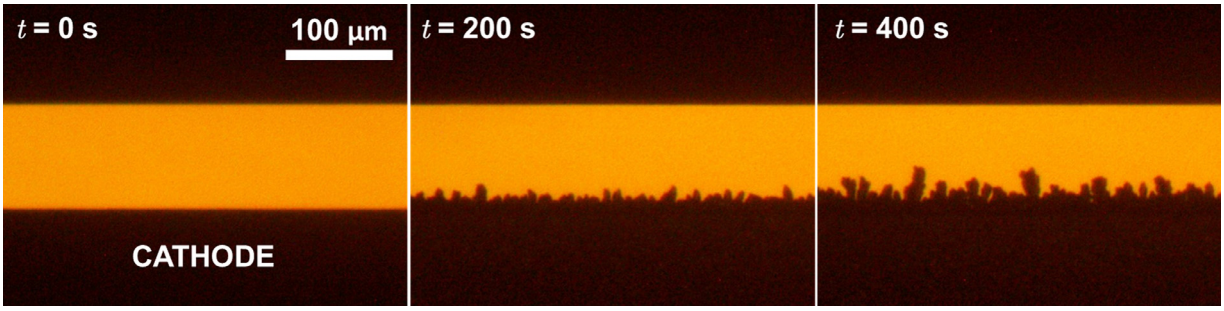

Fig. 7. Evolution of the electrodeposition pattern with time for $\Delta V = 0.25$ V, $L = 100$ µm, and $c_{avg} = 100$ mM. At $t = 200$ s, the pattern is cellular because it was captured before the onset of dendritic growth. Beyond $t = 200$ s, the pattern becomes dendritic and continues to grow in this manner.

due to nonlinear interaction between interface shape and potential gradients, resulting in dendritic forms early, i.e., soon after the inception of the instability. However, by comparison, the potential gradients are steeper in cells of 100 µm spacing (Fig. 6). The sharp potential drop in the 100 µm spacing encourages the pattern to advance in a cellular fashion quickly. This system eventually does become dendritic due to nonlinear interactions between the interface morphology and the electrochemical potential and concentration gradients. However, the electrochemical cells with smaller electrode spacing provide sufficient growth and time for instability analysis at these initial stages. In this work, we have used electrochemical cells with small spacings (100 µm, 1 mm) to enhance diffusional effects, yielding patterns that can be compared favorably with a simple theoretical model described in the SI Appendix.

A total of sixteen experiments were performed using a combination of experimental conditions. Of the sixteen experiments, eight were unique and the other eight were duplicates of the first set. Fig. 7 shows the evolution of the electrodeposition pattern with time for an applied voltage of 0.25 V, 100 µm electrode spacing, and a mean electrolyte concentration of 100 mM. The pattern depicts growth in a cellular manner at the beginning of the deposition that becomes dendritic over time. The pattern of copper deposition on the cathode is typically composed of multiple wavelengths. The growth pattern observed at the initial state before the dendritic forms appear corresponds to the instability explained by the model given in the SI Appendix. For comparison with the model, the image captured just before the onset of dendritic growth was taken for image analysis ($t = 200$ s). After the image analysis routine, the dominant wavelength pattern for this experiment was 43.4 µm.

Few studies have collected comparable data because of the difficulty in isolating morphological patterns. The most relevant work comes from Kahanda et al. [26] and de Bruyn [23]. Kahanda et al. [26] characterized the instability patterns at later stages of electrodeposition through an average root mean square roughness and found the rate of evolution of the pattern interface with time. Their patterns are clearly dendritic with a columnar wavelength of ~ 500 µm. These structures are influenced by non-linear interactions and disturb the forces that form the morphological instability discussed in this work. de Bruyn [23] experimentally measured the growth rate vs wavenumber by capturing the height profiles of deposits under galvanostatic conditions using two parallel electrodes with a very large spacing of 23 mm. The morphological patterns are sensitive to the applied potential. Therefore, a galvanostatic cell will not yield conditions that select one wavelength. The authors noted that the patterns were 'rough,' i.e., dendrites formed soon after the start of deposition. This roughness could be due to potential changes throughout the experiment or possibly due to the large electrode spacing, which we noticed tends to initiate dendrite formation early. Furthermore, the resolution of their images was large (23 µm/pixel), limiting the ability to capture the wavelength predicted by theory (40 µm). These studies demonstrate the challenges associated in operating electrochemical cells that control the forces responsible for morphological instabilities to attain patterns that can be accurately characterized.

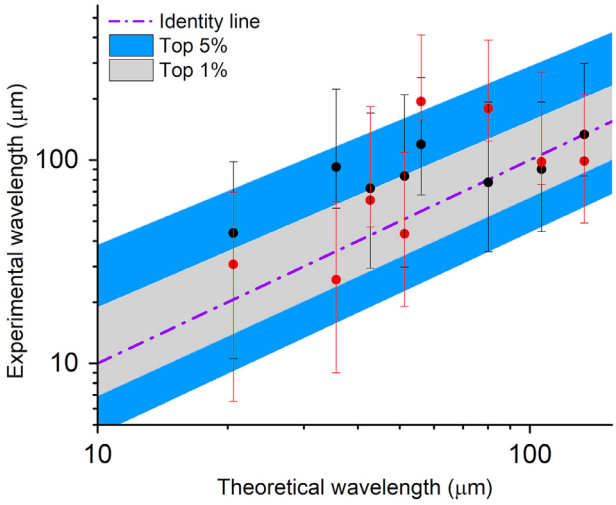

Fig. 8. Comparison of the dominant wavelengths calculated from experiments to the theoretical wavelengths predicted by the model. The dominant wavelengths are calculated from a range of experimental parameters, i.e., electrode spacing (L), applied voltage (ΔV), and mean electrolyte concentration (c_{avg}). Eight experimental conditions are plotted (black circles) with duplicates (red circles). The identity line marks the predicted wavelength corresponding to the maximum growth rate derived from the model for each condition. The wavelength range corresponding to growth rates within 1 and 5% of the maximum growth rate predicted by the model are shown in the gray and blue shaded areas, respectively. The vertical bars across the data points show the wavelength composition obtained from experiments with a 95% confidence interval. (For interpretation of the references to color in this figure legend, the reader is referred to the web version of this article.)

Fig. 8 compares the dominant wavelength measured at different experimental conditions to their respective theoretically-predicted wavelength. The identity line in the plot marks the predicted wavelength corresponding to the maximum growth rate derived from the model for each condition. On account of the broad nature of the σ vs. k^2 plot (see Fig. 2), many wavelengths are expected to be observed during the short timescales of observation. Therefore, regions depicted by wavelengths within 1% (gray region) and 5% (blue region) of the maximum growth rate are also shown. For example, the predicted wavelength of the pattern is 51.3 µm for an applied voltage of 0.25 V, electrode spacing of 100 µm, and mean electrolyte concentration of 100 mM. The predicted wavelength range within 1 and 5% of the maximum growth rates were 34.1 to 94 µm and 22 to 192.4 µm, respectively. Using the image analysis routine, the dominant wavelength calculated for this condition was 43.4 µm, which lies within 1% of the growth rates derived

from the model. Figs. S1(a) and S1(b) in the SI Appendix show similar plots for the entire wavelength composition, including the fundamental and sub-harmonics/harmonics for each experimental condition. As predicted by BuAli et al. [27], the experimental results showed that the dominant wavelength is mainly dependent on the electrode spacing and applied voltage out of the three input variables. The dominant wavelength is observed to increase with electrode spacing and decrease with applied voltage. Meanwhile, the mean electrolyte concentration did not affect the dominant wavelength as much as the other two input variables. Similarly, as predicted by the theoretical model, we saw an increased deposition growth rate with applied voltage from the instability evolution timestamps. Fig. 8 shows that the dominant wavelength for almost all the experiments lies within 5% of the predicted wavelength (blue shaded region). In fact, two-thirds of the experiments yield a dominant wavelength that lies within the 1% region. This exceptional agreement despite the broad growth curve validates the application of linear stability analysis theory in describing the patterns formed during electrodeposition.

4. Conclusions

The slow growth of morphological instabilities formed during electrodeposition leads to the observation of many competing patterns. Rather than evolving to a single wavelength observed in most systems, nonlinear effects lead to the formation of dendrites that obscure the pattern. Design of a microfluidic electrochemical cell enabled better control of the forces responsible for the formation of the instability pattern. The narrow spacings incorporated in the electrochemical cells delay the formation of dendritic branches and allow sufficient time for us to capture the instability pattern before the instability gets obscured. The quasi-1D growth of the instability and the development of a custom noise filter enabled comparison of the initial growth of the instability to an established model. Despite the broad nature of σ vs. k^2 for electrodeposition, we find that the experimental results are clearly within the 5% and largely within the 1% region of the theoretical wavelength range predicted by an instability model (see SI Appendix). Therefore, the experimental results show that the wavelength composition at the onset of electrodeposition instability can be accurately predicted using a simple, heuristic but powerful theory with only two approximations:

1. Interfacial dynamics mainly drive the electrodeposition instability compared to domain dynamics and
2. The electrolyte maintains electroneutrality locally.

Declaration of Competing Interest

The authors declare that they have no known competing financial interests or personal relationships that could have appeared to influence the work reported in this paper.

Credit authorship contribution statement

Sarathy K. Gopalakrishnan: Conceptualization, Methodology, Software, Validation, Formal analysis, Investigation, Data curation, Writing – original draft, Visualization. **Akash Ganesh:** Conceptualization, Methodology, Software, Formal analysis, Investigation. **Chun-Chieh Wang:** Conceptualization, Methodology, Software, Investigation. **Matthew Mango:** Conceptualization, Methodology, Investigation. **Kirk J. Ziegler:** Conceptualization, Methodology, Resources, Writing – review & editing, Supervision, Funding acquisition. **Ranga Narayanan:** Conceptualization, Methodology, Resources, Writing – review & editing, Supervision, Funding acquisition.

Acknowledgment

This work was partially supported by grants from the National Science Foundation NSF-DMR-2004527 and Center for the Advancement of Science in Space (CASIS) AWD01608. The authors also acknowledge financial support from the University of Florida Space Research Initiative, a Dow Chemical Company Foundation Professorship for Kirk J. Ziegler, and the William P. and Tracy Cirioli Professorship for Ranga Narayanan.

Supplementary material

Supplementary material associated with this article can be found, in the online version, at 10.1016/j.electacta.2021.139205 .

References

[1] M. Faraday, On a peculiar class of acoustical figures; and on certain forms assumed by groups of particles upon vibrating elastic surfaces, Phil. Trans. R. Soc. 121 (1831) 299–340, doi:10.1098/rspl.1830.0024.
[2] J.W.S. Rayleigh, On the crispations of fluid resting upon a vibrating support, The London Edinburgh Dublin Philos. Mag. J. Sci. 16 (97) (1883) 50–58, doi:10.1080/14786448308627392.
[3] J.W.S. Rayleigh, Investigation of the character of the equilibrium of an incompressible heavy fluid of variable density, Proc. Lond. Math. Soc. s1-14 (1) (1882) 170–177, doi:10.1112/plms/s1-14.1.170.
[4] J.R. Melcher, G.I. Taylor, Electrohydrodynamics: a review of the role of interfacial shear stresses, Annu. Rev. Fluid Mech. 1 (1) (1969) 111–146, doi:10.1146/annurev.fl.01.010169.000551.
[5] S.R. Coriell, M.R. Cordes, W.J. Boettinger, R.F. Sekerka, Convective and interfacial instabilities during unidirectional solidification of a binary alloy, J. Cryst. Growth 49 (1) (1980) 13–28, doi:10.1016/0022-0248(80)90056-1.
[6] K. Kumar, L.S. Tuckerman, Parametric instability of the interface between two fluids, J. Fluid Mech. 279 (1994) 49–68, doi:10.1017/S0022112094003812.
[7] K. Kumar, Linear theory of Faraday instability in viscous liquids, Proc. Roy. Soc. Lond. A Mat. 452 (1948) (1996) 1113–1126, doi:10.1098/rspa.1996.0056.
[8] S.C. Hardy, S.R. Coriell, Morphological stability and the ice-water interfacial free energy, J. Cryst. Growth 3 (1968) 569–573, doi:10.1016/0022-0248(68)90225-X.
[9] T.B. Benjamin, F.J. Ursell, The stability of the plane free surface of a liquid in vertical periodic motion, Proc. R. Soc. Lon. Ser-A 225 (1163) (1954) 505–515, doi:10.1098/rspa.1954.0218.
[10] W. Batson, F. Zoueshtiagh, R. Narayanan, The Faraday threshold in small cylinders and the sidewall non-ideality, J. Fluid Mech. 729 (496-523) (2013) 9, doi:10.1017/jfm.2013.324.
[11] D.S. Pillai, R. Narayanan, Rayleigh–Taylor stability in an evaporating binary mixture, J. Fluid Mech. 848 (2018), doi:10.1017/jfm.2018.385.
[12] K. Ward, F. Zoueshtiagh, R. Narayanan, Faraday instability in double-interface fluid layers, Phys Rev. Fluids 4 (4) (2019) 043903, doi:10.1103/PhysRevFluids.4.043903.
[13] N. Brosius, K. Ward, S. Matsumoto, M. SanSoucie, R. Narayanan, Faraday forcing of high-temperature levitated liquid metal drops for the measurement of surface tension, NPJ Microgravity 4 (1) (2018) 1–5, doi:10.1038/s41526-018-0044-1.
[14] B. Dinesh, R. Narayanan, Branching behaviour of the Rayleigh–Taylor instability in linear viscoelastic fluids, J. Fluid Mech. 915 (2021), doi:10.1017/jfm.2021.80.
[15] L.E. Johns, R. Narayanan, Interfacial Instability, Springer, 2002, doi:10.1007/978-3-642-27758-0_724-2.
[16] J.D. Zahn, Interfacial Instability, Springer US, Boston, MA, 2008, doi:10.1007/978-0-387-48998-8_724.
[17] J.W. Rutter, B. Chalmers, A prismatic substructure formed during solidification of metals, Can. J. Phys. 31 (1) (1953) 15–39, doi:10.1139/p53-003.
[18] F. Sagués, M.Q. López-Salvans, J. Claret, Growth and forms in quasi-two-dimensional electrocrystallization, Phys. Rep. 337 (1-2) (2000) 97–115, doi:10.1016/S0370-1573(00)00057-0.
[19] C. Léger, L. Servant, J.L. Bruneel, F. Argoul, Growth patterns in electrodeposition, Proceedings of the 20th IUPAP International Conference on Statistical Physics, Phys. A 263 (1) (1999) 305–314, doi:10.1016/S0378-4371(98)00484-1.
[20] M.-Q. Lopez-Salvans, P.P. Trigueros, S. Vallmitjana, J. Claret, F. Sagués, Fingerlike aggregates in thin-layer electrodeposition, Phys. Rev. Lett. 76 (21) (1996) 4062, doi:10.1103/PhysRevLett.76.4062.
[21] D.P. Barkey, R.H. Muller, C.W. Tobias, Roughness development in metal electrodeposition: I. Experimental results, J. Electrochem. Soc. 136 (8) (1989a) 2199–2207, doi:10.1149/1.2097258.
[22] D.P. Barkey, R.H. Muller, C.W. Tobias, Roughness development in metal electrodeposition: II. Stability theory, J. Electrochem. Soc. 136 (8) (1989b) 2207–2214, doi:10.1149/1.2097260.
[23] J.R. de Bruyn, Early stages of ramified growth in quasi-two-dimensional electrochemical deposition, Phys. Rev. E. 53 (1996) R5561–R5564, doi:10.1103/PhysRevE.53.R5561.

[24] J.R. de Bruyn, Physical and electrochemical contributions to the cell voltage in the thin-layer electrochemical deposition of copper at constant current, Phys. Rev. Lett. 56 (1997) 3326–3337, doi:10.1103/PhysRevE.56.3326.
[25] J. Elezgaray, C. Léger, F. Argoul, Linear stability analysis of unsteady galvanostatic electrodeposition in the two-dimensional diffusion-limited regime, J. Electrochem. Soc. 145 (6) (1998) 2016–2024, doi:10.1149/1.1838592.
[26] G. Kahanda, X.-q. Zou, R. Farrell, P.-z. Wong, Columnar growth and kinetic roughening in electrochemical deposition, Phys. Rev. Lett. 68 (1992) 3741–3744, doi:10.1103/PhysRevLett.68.3741.
[27] Q. BuAli, L.E. Johns, R. Narayanan, The growth of roughness during electrodeposition, Electrochim. Acta 51 (14) (2006) 2881–2889, doi:10.1016/j.electacta.2005.08.020.
[28] L.-G. Sundström, F.H. Bark, On morphological instability during electrodeposition with a stagnant binary electrolyte, Electrochim. Acta 40 (5) (1995) 599–614, doi:10.1016/0013-4686(94)00379-F.
[29] P. Schilardi, S. Méndez, R.C. Salvarezza, A.J. Arvia, Evolution of the growth front for copper electrodeposition followed by real time imaging, Langmuir 14 (15) (1998) 4308–4314, doi:10.1021/la971358k.
[30] K.I. Popov, N. Nikolić, Z.L. Rakočević, The estimation of solid copper surface tension in copper sulfate solutions, J. Serb. Chem. Soc. 67 (11) (2002) 769–775, doi:10.2298/JSC0211769P.
[31] Z. Zong, H. Yu, L. Nui, M. Zhang, C. Wang, W. Li, Y. Men, B. Yao, G. Zou, Potential-induced copper periodic micro-/nanostructures by electrodeposition on silicon substrate, Nanotechnology 19 (31) (2008) 315302, doi:10.1088/0957-4484/19/31/315302.
[32] K. Wang, L. Niu, Z. Zong, M. Zhang, C. Wang, X. Shi, Y. Men, G. Zou, Direct electrodeposition of copper ladder structures on a silicon substrate, Cryst. Growth Des. 8 (2) (2008) 442–445, doi:10.1021/cg070200n.
[33] H. Kim, J.G. Kim, J.W. Park, C.N. Chu, Selective copper metallization of nonconductive materials using jet-circulating electrodeposition, Precis. Eng. 51 (2018) 153–159, doi:10.1016/j.precisioneng.2017.08.005.
[34] J.O. Bockris, A.K.N. Reddy, M. Gamboa-Aldeco, Modern Electrochemistry 2A: Fundamentals of Electrodics, Springer US, 2000, doi:10.1007/0-306-47605-3_2.
[35] M. Haataja, D.J. Srolovitz, A.B. Bocarsly, Morphological stability during electrodeposition, J. Electrochem. Soc. 150 (10) (2003) C699, doi:10.1149/1.1602455.
[36] C.P. Nielsen, H. Bruus, Morphological instability during steady electrodeposition at overlimiting currents, Phys. Rev. E. 92 (2015) 052310, doi:10.1103/PhysRevE.92.052310.
[37] R.A. Enrique, S. DeWitt, K. Thornton, Morphological stability during electrodeposition, MRS Commun. 7 (2017) 658–663, doi:10.1557/mrc.2017.38.
[38] R. Aogaki, T. Makino, Theory of powdered metal formation in electrochemistry-morphological instability in galvanostatic crystal growth under diffusion control, Electrochim. Acta 26 (11) (1981) 1509–1517, doi:10.1016/0013-4686(81)85123-7.
[39] M.D. Pritzker, T.Z. Fahidy, Morphological stability of a planar metal electrode during potentiostatic electrodeposition and electrodissolution, Electrochim. Acta 37 (1) (1992) 103–112, doi:10.1016/0013-4686(92)80018-H.
[40] S. Chandrasekhar, Hydrodynamic and Hydromagnetic Stability, Courier Corporation, 2013.
[41] S.W. Smith, The Scientist and Engineer's Guide to Digital Signal Processing, California Technical Publishing, USA, 1997.
[42] N. Otsu, A threshold selection method from gray-level histograms, IEEE Trans. Syst. Man. Cyb. 9 (1) (1979) 62–66, doi:10.1109/TSMC.1979.4310076.
[43] D. Bradley, G. Roth, Adaptive thresholding using the integral image, J. Graph. Tools 12 (2) (2007) 13–21, doi:10.1080/2151237X.2007.10129236.
[44] R.W. Johnson, An introduction to the bootstrap, Teach. Stat. 23 (2) (2001) 49–54, doi:10.1111/1467-9639.00050.
[45] D.E. Brunetti B, About estimating the limit of detection by the signal to noise approach, Pharm. Anal. Acta 06 (04) (2015) 4, doi:10.4172/2153-2435.1000355.
[46] T. Sheehan, R.A. Yost, What's the most meaningful standard for mass spectrometry: instrument detection limit or signal-to-noise ratio, Curr. Trends Mass. Spectrom. 13 (2015) 16–22. URL https://www.spectroscopyonline.com/view/vol-13-no-4-current-trends-mass-spectrometry-october-2015-issue-pdf-0
[47] R.K. Bramley, D.G. Bullock, J.R. Garcia, Quality Control and Assessment, Pharmaceutical Press, 2008.
[48] U. Şengül, Comparing determination methods of detection and quantification limits for aflatoxin analysis in hazelnut, J. Food Drug Anal. 24 (1) (2016) 56–62, doi:10.1016/j.jfda.2015.04.009.
[49] G. Marshall, P. Mocskos, H.L. Swinney, J.M. Huth, Buoyancy and electrically driven convection models in thin-layer electrodeposition, Phys. Rev. E. 59 (1999) 2157–2167, doi:10.1103/PhysRevE.59.2157.
[50] M.D. Tikekar, G. Li, L.A. Archer, D.L. Koch, Electroconvection and morphological instabilities in potentiostatic electrodeposition across liquid electrolytes with polymer additives, J. Electrochem. Soc. 165 (16) (2018) A3697–A3713, doi:10.1149/2.0271816jes.
[51] S.M. Rubinstein, G. Manukyan, A. Staicu, I. Rubinstein, B. Zaltzman, R.G.H. Lammertink, F. Mugele, M. Wessling, Direct observation of a nonequilibrium electro-osmotic instability, Phys. Rev. Lett. 101 (2008) 236101, doi:10.1103/PhysRevLett.101.236101.
[52] M. Frigo, S.G. Johnson, FFTW: an adaptive software architecture for the FFT, in: Proceedings of the 1998 IEEE International Conference on Acoustics, Speech and Signal Processing, ICASSP '98 (Cat. No.98CH36181), vol. 3, 1998, pp. 1381–1384, doi:10.1109/ICASSP.1998.681704.